MRS Communications (2018), *8*, 1029–1036
© Materials Research Society, 2018
doi:10.1557/mrc.2018.133

MRS Communications

Research Letter

Localized plasmonic fields of nanoantennas enhance second harmonic generation from two-dimensional molybdenum disulfide

Gregory T. Forcherio, MicroElectronics-Photonics Program, University of Arkansas, Fayetteville, AR 72701, USA; Sensors & Electron Devices Directorate, U.S. Army Research Laboratory, Adelphi, MD 20783, USA
Luigi Bonacina, and **Jean-Pierre Wolf,** Applied Physics Departement, Université de Genève, Genève 1211, Switzerland
D. Keith Roper, MicroElectronics-Photonics Program, University of Arkansas, Fayetteville, AR 72701, USA; Ralph E. Martin Department of Chemical Engineering, University of Arkansas, Fayetteville, AR 72701, USA

Address all correspondence to G. T. Forcherio at **gregory.t.forcherio.ctr@mail.mil**

(Received 30 May 2018; accepted 5 July 2018)

Abstract

Frequency-dependence and magnitude of second harmonic generation (SHG) from ~4×10^5 nm^2 molybdenum disulfide (MoS_2) monolayers was examined in presence of single 150 nm plasmonic gold@silica shell@core nanoantenna monomer and dimers. Quantitative agreement between discrete dipole approximation-calculated fields and measured SHG enhancements was found. SHG from MoS_2 was enhanced up to 1.88× upon deposition of a plasmonic nanoantenna-dimer with 170 nm gap, reaching maximal normalized SHG conversion efficiency of 0.0250%/W. Pump losses attributable to plasmonic damping, e.g., scattering and/or hot-electron injection into MoS_2, were apparent. Linear and nonlinear optical activity of MoS_2 and nanoantenna controls were compared with literature values.

Introduction

Transition metal dichalcogenide (TMD) monolayers are promising optoelectronic platforms because of their direct bandgap near 2 eV and 10^2 pm/V second-order nonlinear susceptibility, $\chi^{(2)}$. Interfacing monolayer TMD with metal nanoantennas offers additional degrees of freedom in design of optoelectronics via surface plasmon light manipulation. Examination of optoelectronic processes in nanoantenna-TMD heterostructures has to date focused on linear optical operations, where polarization, $\boldsymbol{P}$, responds linearly to the excitation field $\boldsymbol{E}_\omega$ at a frequency ω according to $\chi^{(1)}$. As examples, far-field optical absorption and scattering activity,[1] 10–1000× enhanced TMD absorption/emission,[2] photoluminescence (PL) quenching,[3] and 11–38% efficient plasmonic hot electron transport[4,5] have been reported. Extraordinary second harmonic generation (SHG) and frequency mixing have been measured from two-dimensional (2D) TMD arising from the second-order nonlinear contribution to $\boldsymbol{P}$ that scales with $\boldsymbol{E}_\omega^2$ according to their large $\chi^{(2)}$.[6–10] Although SHG and third harmonic generation (THG) have been demonstrably augmented 60–1700× by plasmonic fields in many nanomaterial heterostructures,[11–17] such activity remains largely unexplored for nanoantenna-TMD systems.

Fryett et al. first reported 200× enhancement of SHG from a sub-region of mechanically-exfoliated monolayer tungsten diselenide (WSe_2) by a linearly-polarized Si cavity photonic crystal, after deconvoluting SHG from background PL bands.[10,18] Enhanced SHG was ostensibly due to the augmented $\boldsymbol{E}_\omega$ strength from the photonic cavity crystal. Wang et al. later used selective excitation of lateral gap plasmons within 20 nm trenches of a Au film that supported a WSe_2 monolayer to point-wise enhance SHG 47× within the trench sub-regions, and 7000× relative to WSe_2 on sapphire.[19] Equation (1) classically describes SHG intensity, $I_{2\omega}$, for such heterostructures in the absence of SHG contributions from the resonator component:

$$I_{2\omega} = \frac{\pi^2 c \epsilon_o}{2 n_\omega^2 n_{2\omega} \lambda_\omega^2} \left[\chi_{2\omega}^{(2)}\right]^2 L^2 \left(\gamma |\boldsymbol{E}_\omega|\right)^4 \quad (1)$$

according to constants (free-space permittivity, ϵ_o; speed of light, c), nonlinear source material parameters ($\chi_{2\omega}^{(2)}$; linear refractive index, n; thickness, L), the pump field strength, E_ω, at wavelength λ_ω, and a field augmentation factor, γ, induced by the single-mode resonator component.

This work examines enhanced SHG from ~4×10^5 nm^2 molybdenum disulfide (MoS_2) monolayers in the presence of localized surface plasmon resonances (LSPR) excited on *single* 150 nm gold@silica ($Au@SiO_x$) shell@core nanoantenna monomers and dimers using a tunable Ti:Sapphire-pumped multiphoton microscope and discrete dipole approximation (DDA). The $Au@SiO_x$ nanoantenna(s) and MoS_2 function as the single-mode resonator(s) and nonlinear source material in this work, respectively. Results in the forthcoming sections are organized as follows:

https://doi.org/10.1557/mrc.2018.133 Published online by Cambridge University Press

(1) Raw SHG data for MoS_2 with a single $Au@SiO_x$ nanoantenna
(2) Control experiments for $Au@SiO_x$ nanoantennas and MoS_2
(3) SHG enhancement from MoS_2 by two different $Au@SiO_x$ nanoantenna dimers
(4) Calculated SHG conversion efficiencies for each $Au@SiO_x$ nanoantenna-MoS_2 heterostructure.

Results

$Au@SiO_x$ shell@core nanoantennas were drop-cast onto MoS_2 monolayers (~1 μm edge length, 4×10^5 nm^2 area) fabricated via chemical vapor deposition (CVD) onto silicon (Si) wafer with 300 nm oxide (CVD-MOS2; 2Dsemiconductors, Scottsdale, AZ, USA). Figure 1(a) shows a scanning electron microscopy (SEM; Philips XL40, FEI, Hillsboro, OR, USA) micrograph of MoS_2, with PL inset revealing a 1.86 eV maxima coinciding with the A exciton transition. The 148 ± 8 nm overall diameter $Au@SiO_x$ nanoantennas had a 15 ± 6 nm Au shell on a 120 nm SiO_x core (lot MGM1774; nanoComposix, San Diego, CA, USA). Figures 1(b) shows a SEM micrograph of a representative $Au@SiO_x$-MoS_2 monomeric heterostructure. Scanning transmission electron microscopy (STEM; Tecnai F-20, FEI, Hillsboro, OR, USA) analysis, inset in Fig. 1(b), revealed the core-shell architecture of the $Au@SiO_x$ nanoantenna. Stochastic deposition of nanoantennas by the drop-cast protocol resulted in isolated $Au@SiO_x$ nanoantennas and MoS_2 monolayers, in addition to the heterostructures, within the same sample. Particular isolated nanoantennas and monolayers were analyzed independently as negative controls. Figure 1(c) shows enhanced optical near-field intensity, $\gamma^2 = |\boldsymbol{E}/\boldsymbol{E}_o|^2_\omega$, at the 820 nm dipole LSPR of a monomeric heterostructure calculated using DDA solutions to Maxwell's equations. Figure 1(d) shows the calculated linear extinction spectra, absent any nonlinear interaction. Exciton transitions and LSPR features in the spectra are labeled. Details of computation, fabrication, and microscopic/spectroscopic characterization are in the Supplementary Material.

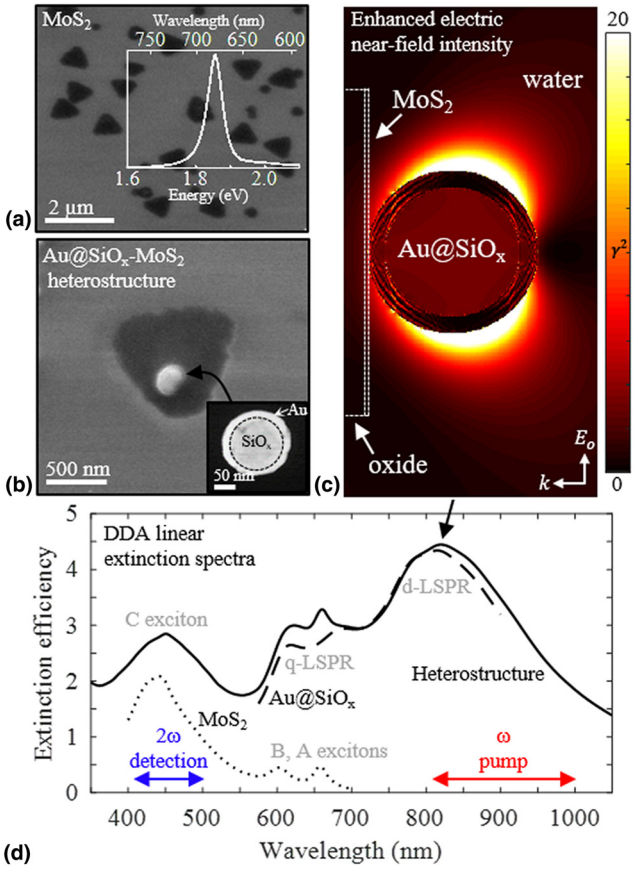


Figure 1. (a) SEM micrograph of CVD MoS_2 on a Si wafer and PL from 488 nm excitation (inset). (b) SEM micrograph of a representative $Au@SiO_x$-MoS_2 heterostructure. Inset is a STEM image of a single $Au@SiO_x$ nanoantenna with labeled Au shell and SiO_x core. Accelerating voltages in SEM and STEM were 5 and 120 kV, respectively. (c) Enhanced optical intensity factor, $\gamma^2 = |\boldsymbol{E}/\boldsymbol{E}_o|^2_\omega$, in the heterostructure excited at the 820 nm dipole LSPR mode of the nanoantenna. The scale was truncated to a maximum of 20 from a simulated high value near 60 to emphasize the dipole pattern. (d) Calculated linear optical extinction spectra via DDA for a $Au@SiO_x$-MoS_2 heterostructure (solid), single $Au@SiO_x$ nanoantenna (dashed), and a MoS_2 monolayer (dotted), each on a silica substrate and immersed in water. Resonant modes of the system (gray text) and pump/detection frequencies from which SHG was experimentally interrogated are labeled.

Enhanced SHG from microscale MoS_2 by a single $Au@SiO_x$ nanoantenna

SHG from monolayer MoS_2 in the presence of a single $Au@SiO_x$ nanoantenna was measured with a laser-scanning multiphoton microscope (A1R-MP; Nikon Instruments Europe, Amsterdam, NLD) coupled to a wavelength tunable, 100 fs Ti:Sapphire laser (MaiTai Deep See; Spectra-Physics, Santa Clara, CA, USA). Figure 2 shows detected spectra arising from 810 to 1000 nm ω excitation of a CVD-synthesized, ~4×10^5 nm^2-area MoS_2 monolayer in the absence (gray) and presence (red) of one 150 nm $Au@SiO_x$ nanoantenna at its center. Scattered photons were collected by a 60×, 1.27 NA water-immersion objective and delivered to a photomultiplier tube (PMT) array at 2.5 nm wavelength binning. Corresponding SEM and SHG micrographs are shown above; arrows correlate each SHG micrograph with its associated spectra. Inset confirms second-order nonlinear behavior with a 1.8 power-dependence for the heterostructure. It is noted SHG remains finite at pump wavelengths less than 810 nm and greater than 1000 nm, but acquisition conditions were optimized for this spectral range.

Integrated SHG intensity from the ~4×10^5 nm^2 MoS_2 area was enhanced 17–84% across the spectrum in the presence of a single 150 nm $Au@SiO_x$ nanoantenna, ostensibly due to the surface plasmon-augmented local field. This was despite the relatively small ~5–10% MoS_2 surface area shadowed by the nanoantenna, estimated from SEM. At conditions evaluated, ~90–95% of the MoS_2 monolayer did not experience local field augmentation by the nanoantenna. Previous reports of plasmon-enhanced SHG citing order-of-magnitude

https://doi.org/10.1557/mrc.2018.133 Published online by Cambridge University Press

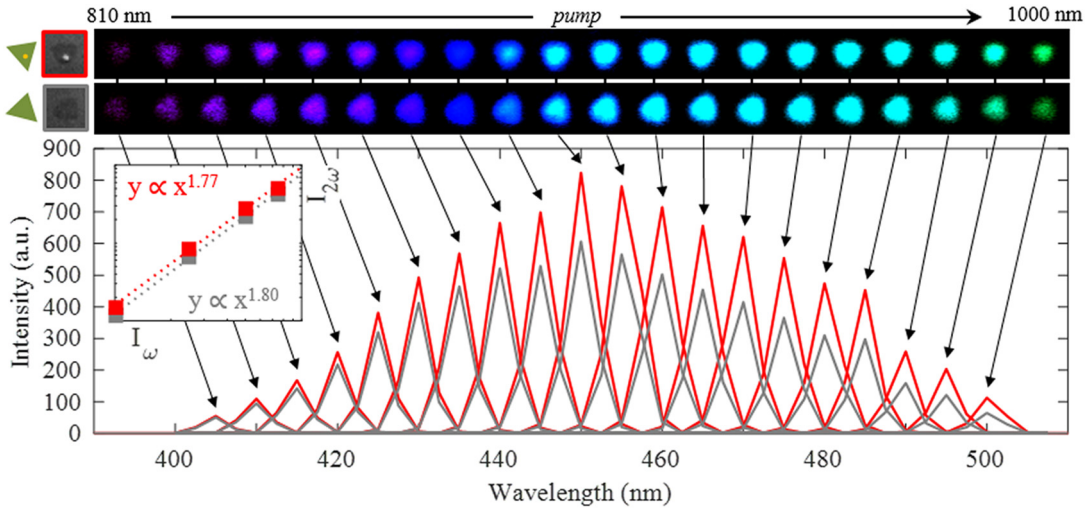


Figure 2. Scattered SHG (per unit area) spectra from a MoS_2 monolayer, ~4×10^5 nm^2 area, at 810–1000 nm excitation (10 nm step) in the absence (gray) and presence (red) of a single Au@SiO_x nanoantenna (15 nm Au shell; 120 nm SiO_x core). The inset shows 1.77- and 1.80-power dependence between SH and pump intensities taken at 880 nm excitation, confirming a second-order nonlinear process for the heterostructure and MoS_2 control, respectively. SEM and SHG micrographs at each excitation wavelength are shown (top) with arrows to corresponding spectra.

improvements in SHG signal at the LSPR consider (i) a nonlinear medium doped isotropically with nanoantennas or a lithographed nanoantenna lattice or (ii) local, point-wise SHG data. Highest MoS_2 SHG enhancements by the single nanoantenna here were observed off-resonance, away from its LSPR. In contrast, maximal MoS_2 SHG enhancement by Au@SiO_x nanoantenna dimers was near their LSPR (discussed in forthcoming sections). It is hypothesized that off-LSPR occurrence of the maximal SHG enhancement was in part due to plasmonic losses, which consequently caused different laser excitation conditions for TMD at each pump wavelength. Putative dampening of laser energy by plasmonic activity on nanoantenna could arise from: in-plane scattering away from TMD and/or transduction into Landau-damped hot electrons injected into TMD (approximately 11–38% of LSPR dephasing),[4,5] for example. Such plasmonic losses alter how the pump laser couples with the MoS_2, but are neglected for simplicity in Eq. (1) and will be discussed in more detail in forthcoming sections. SHG from MoS_2 and Au@SiO_x nanoantenna controls are discussed in the proceeding section to provide context for enhanced SHG from the heterostructures.

MoS_2 and Au@SiO_x nanoantenna control experiments

Mean SHG intensity measured from ten distinct MoS_2 monolayers exhibited a frequency-dependence corresponding with the expanded density of states along the C exciton transitions.[20] The C transition is associated with the van Hove singularity of MoS_2. Malard et al. also measured an association of SHG in this spectral range to the direct C exciton transition near the Γ point at approximately 2.8 eV (450 nm).[7] Figure 3(a) shows the frequency-dependence of SHG from 810 to 1000 nm ω excitation averaged from ten crystals (black squares). Superimposed are DDA-calculated bulk-like $\left[\chi^{(2)}_{2\omega}\right]^2$ spectra [black dashed line; proportional to SHG via Eq. (1)] and measured linear differential reflectance spectra (blue solid line) of the MoS_2, revealing the C transition. The C transition concomitantly acts as a loss (via absorption of SH signal) and as a SHG gain (via $\chi^{(2)}$ resonance).[7] SHG intensity did not decrease over time, indicating no photodamage. Power dependence of SHG exhibited typical quadratic behavior.

Measured SHG profile for undecorated MoS_2 monolayers aligned closely with DDA-simulated bulk-like $\chi^{(2)}_{2\omega}$ (black dashed line), which was based on Miller's rule using linear MoS_2 susceptibility, $\chi^{(1)}$, as detailed in the Supplementary Material. The measured C exciton transition (blue line) occurred 15 nm blue-shifted from the 450 nm SHG maximum, consistent with measurements by Malard et al.[7] Density functional theory (DFT) calculations and a Bethe-Salpeter exciton model of $\chi^{(2)}$ for MoS_2 corroborate the measured SHG trends.[6,21,22] This is illustrated in Fig. S7. An approximate 7 nm offset between SHG maximum and simulated bulk-like $\left[\chi^{(2)}_{2\omega}\right]^2$ was attributable to the water environment of the immersion-objective used here versus the air environment[23] of the MoS_2 sample used to obtain linear dielectric data by Mukherjee et al.[24] from which $\chi^{(2)}_{2\omega}$ was derived via DDA. Polarization-resolved SHG from the MoS_2 to elucidate depolarization or crystal axis orientation was not measured herein but has been well-characterized elsewhere.[6,7]

Isolated Au@SiO_x nanoantennas atop SiO_x exhibited broadband 2ω luminescence when excited across the ω wavelength range of 810–1000 nm, whereas SHG was observed from

https://doi.org/10.1557/mrc.2018.133 Published online by Cambridge University Press

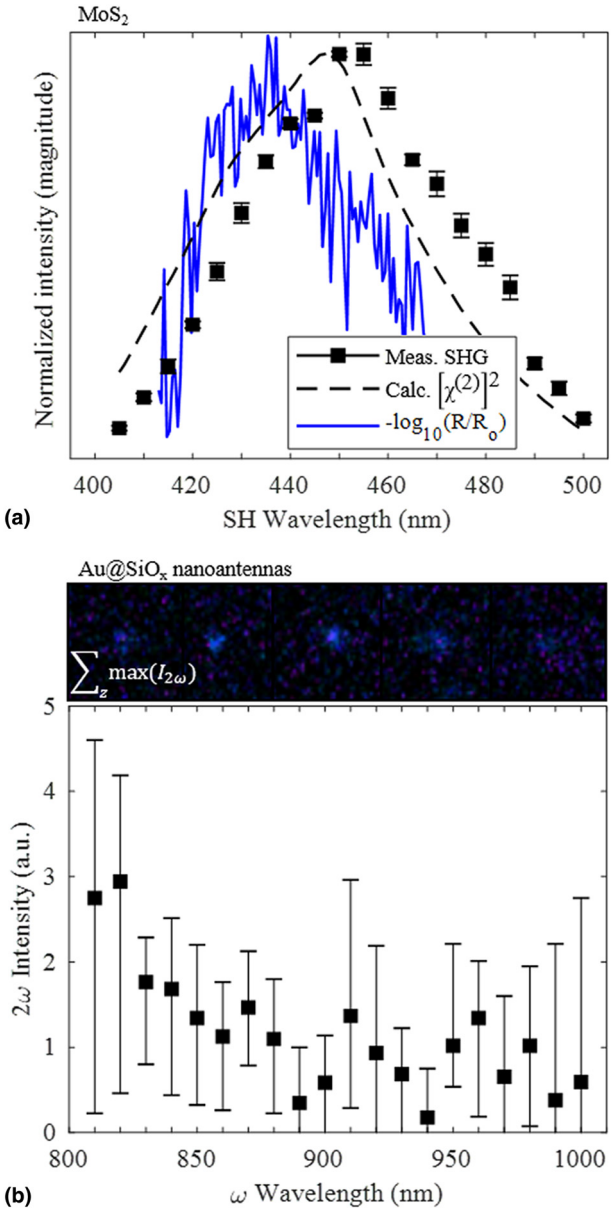


Figure 3. SHG control experiments. (a) Normalized SHG intensity (integrated over SH bandwidth) versus central SH wavelength averaged from ten distinct MoS_2 monolayers (black squares). Superimposed are bulk-like $\left[\chi^{(2)}_{2\omega}\right]^2$ magnitude calculated DDA (black dashed line) and measured differential reflectance spectra (blue line) for MoS_2 monolayers. (b) Mean 2ω emission intensity (per unit area) for five distinct Au@SiO_x nanoantennas (15 nm Au shell; 120 nm SiO_x core). The top panel shows 2ω images of the five individual Au@SiO_x nanoantennas according to summed, maximum 2ω luminescence from 400 to 480 nm detected within a 5 μm z-scan using 820 nm excitation. Error in each graph reflects the maximum and minimum from the mean.

MoS_2. This was attributable to interband relaxation of *d*-orbital electrons in the Au[25] rather than SHG originating from the nanoantenna. Figure 3(b) shows the mean detected intensity in the 2ω spectrum from five Au@SiO_x nanoantennas; intensity magnitude was negligible compared with that of MoS_2 SHG in Fig. 2. The centrosymmetric fcc structure of Au and amorphous SiO_x prohibited SHG beyond minute surface contributions, where crystalline symmetry is inherently broken. Luminescence decreased as ω was detuned from the 817 nm dipole LSPR, consistent with the LSPR profile in Fig. 1(d) and other reports.[15] Broadband luminescence has been widely noted for high-fluence laser excitation of metal nanoantennas.[25] Multiphoton identification of single Au@SiO_x nanoantennas, corroborated independently with SEM, was facilitated by a secondary method of multiphoton image acquisition where maximal detected 400–480 nm luminescence from 820 nm excitation across a 5 μm z-scan was translated into a 2D projection [see top of Fig. 3(b) and Fig. S5].

SHG from nanoantennas has been shown to increase with the degree of non-centrosymmetry in antenna geometry. For example, Walsh et al. enhanced SHG 40 × from Au nanocylinder arrays by plasmon-phonon transduction at various laser intensities to introduce morphological disorder into the otherwise centrosymmetric cylinders.[26] Augmentation of surface SHG by plasmon-enhanced local electric fields is an alternative mechanism that has been studied.[27] The Au@SiO_x nanoantennas studied herein had centrosymmetric core-shell morphology that resulted in negligible SHG with no appreciable surface contribution.

Enhanced SHG from MoS_2 by Au@SiO_x nanoantenna dimers

SHG intensity from MoS_2 monolayers was enhanced in presence of Au@SiO_x nanoantenna dimers, ostensibly due to augmentation of the local electric field governed by the inter-nanoantenna gap within the dimer. Figure 4 shows the measured SHG intensity enhancement factors, X, by a Au@SiO_x nanoantenna dimer with 280 nm (blue) or 170 nm (black) gap, relative to two comparably sized MoS_2 controls. Corresponding SEM micrographs are inset. Overall SHG gain was low. Likewise, Metzger et al. cited difficulty in clearly resolving THG gain from an indium tin oxide nanoparticle placed within a resonating plasmonic Au nanodimer.[17] Linear extinction spectra calculated by DDA for each nanoantenna dimer suspended in water (due to water immersion objective) are superimposed onto the measured X values. Trend and relative magnitudes of the measured X values were consistent with their respective nanoantenna dimer extinction spectra. Field strength between nanoantenna dimer elements increases exponentially as gap size narrows due to capacitive coupling.[28] Power-dependence of SHG was measured to be 1.87 and 1.82 for 280 and 170 nm gap dimers, respectively. Error bars reflect maximum and minimum from the mean due to minute variation in the size of MoS_2 controls.

Enhancement of SHG from MoS_2 at the Au@SiO_x LSPR was highest for the 170 nm gap dimer, reaching up to 88% (i.e., $X = 1.88$) at 810 nm. Expanding the gap to 280 nm decreased X to 74%, which is consistent with reduced coupling as the two Au@SiO_x nanoantenna comprising the dimer

https://doi.org/10.1557/mrc.2018.133 Published online by Cambridge University Press

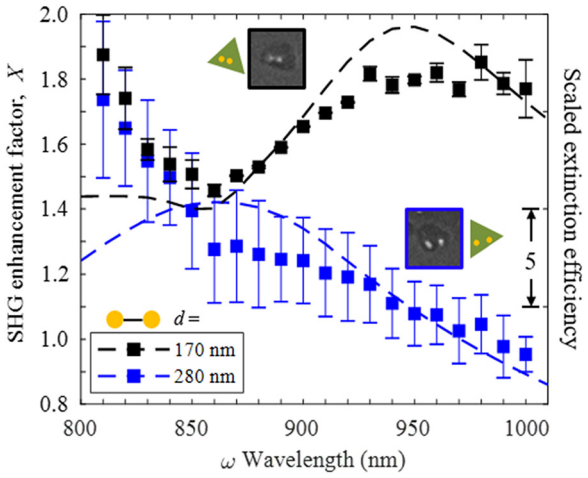


Figure 4. Measured SHG enhancement factor, *X*, for MoS_2 monolayers, each ~4×10^5 nm^2 in area, by nanoantenna dimers composed of 150 nm Au@SiO_x (15 nm Au shell; 120 nm SiO_x core) separated by 170 nm (black) and 280 nm (blue). Error reflects the maximum and minimum from the mean enhancement over two nearby, comparably-sized MoS_2 controls. One dimer was measured for each gap distance. Superimposed are DDA-calculated linear extinction spectra (dashed lines) for MoS_2-free Au@SiO_x chains in water with spacing equal to each measured dimer gap, and was scaled to show correlation with their respective *X* profile. SEM micrographs for each dimeric heterostructure are shown.

separate. SHG enhancement by the 280 nm gap dimer decreased as ω was detuned from the LSPR. The decrease coincided DDA-calculations of optical field intensity enhancement factors, i.e., γ^2, at the MoS_2 monolayer by the LSPR (see Fig. S13). For the 170 nm gap dimer, however, *X* increased beyond 860 nm excitation in correspondence with the emergence of a second plasmon resonance near 960 nm arising from the capacitive interaction. The emergence of capacitively-coupled plasmon resonances at energies lower than the single-particle LSPR has also been observed elsewhere.[28] DDA simulation of parallel-polarized excitation of single Au@SiO_x nanoantennas arranged in a chain with 170 nm gap confirmed the emergence of such a coupled resonance (see the black dashed line in Fig. 4 and black solid line in Fig. S11). Higher *X* exhibited by the 170 nm gap dimer in the 800–890 nm range relative to the 280 nm gap dimer appears counter to the absolute, MoS_2-absent extinction magnitudes of the nanoantenna dimers shown in Fig. S11. However, their true optical extinction could differ upon the inclusion of the MoS_2 (prohibitive computationally, detailed later) and the local field around a nanoantenna differs from the field at its interface with a MoS_2 sublayer.

Normalized SHG conversion efficiency analysis

Measured enhancement of MoS_2 SHG in the presence of Au@SiO_x nanoantennas, *X*, was consistent with augmentation of the local electric field by LSPR excitation, quantified numerically by a factor $\gamma = |\boldsymbol{E}/\boldsymbol{E}_o|_\omega$. Overall SHG conversion efficiency is proportional to γ^4, as in Eq. (1).[12] An *ab initio* estimate of overall SHG conversion efficiency, $\eta_{2\omega}$, for MoS_2 in the absence of a nanoantenna was calculated to be up to 7.8×10^{-8} at the 100 GW/cm^2 irradiation intensity used herein, per Eqs. (2) and (3) (derived in §S8 of the Supplementary Material) under the following assumptions:[29] (i) interaction length, $L = 6.5$ Å for monolayer MoS_2, was within the focus depth; (ii) no pump depletion by the MoS_2; (iii) phase coherence; and (iv) bulk-like $\chi^{(2)}_{2\omega}$ for monolayer MoS_2 calculated from a Miller's rule calculation with DDA (see Supplementary Material):

$$\eta_{2\omega} \equiv \frac{I_{2\omega}}{I_\omega} = \eta_{\text{norm}} L^2 I_\omega \tag{2}$$

$$\eta_{\text{norm}} \equiv \frac{2\pi^2 \left[\chi^{(2)}_{2\omega}\right]^2}{n^2_\omega n_{2\omega} c \epsilon_o \lambda^2_\omega} \tag{3}$$

Here, the normalized SHG conversion efficiency, η_{norm}, is introduced to allow direct comparison of SHG performance with other materials or heterostructures by removing dependence on extrinsic parameters I_ω and *L*.[29] Absolute determination of $\eta_{2\omega}$ using measured values of $I_{2\omega}$ and I_ω was precluded by the absence of rigorously characterized signal losses within the microscope (e.g., ω-dependent losses at each lens/mirror, PMT quantum efficiencies, etc.).

Figure 5 shows η_{norm} for an isolated MoS_2 monolayer (gray line) calculated by Eq. (3) using the DDA-calculated bulk-like $\chi^{(2)}$ via Miller's rule, which closely matches the measured intensity profile in Fig. 3. Equation (3) accounts for the wavelength and optical dispersion at the ω and 2ω frequencies, respectively, which advances an interpretation of SHG spectrum profiles beyond only $\chi^{(2)}$. The undecorated MoS_2 had a calculated peak η_{norm} of 0.0159%/W. By comparison, lithium niobate technology performs near 0.0001%/W.

Full-field DDA calculations indicated the presence of a single Au@SiO_x nanoantenna as a passive SHG gain element could increase peak η_{norm} to 0.0239%/W, labeled as $\gamma^4\eta_{\text{norm}}$ [red line; see Eq. (1) and (S5)–(S7)]. This calculation assumed the nanoantenna (i) did not contribute SHG (confirmed earlier) and (ii) passively enhanced MoS_2 η_{norm} according to its local plasmonic field factor, γ. In the latter, γ^2 incident upon the MoS_2 was calculated by DDA at each ω. Although γ^2 "seen" by the MoS_2 from interaction with the nanoantenna followed the LSPR spectral profile in Fig. 1(d), its magnitude remained within ±5% across the 810–1000 nm excitation spectrum, as detailed in Fig. S13.

Plasmonic field-augmentation appeared responsible for the measured SHG enhancements from MoS_2. This was implied by a heuristic comparison in Fig. 5 between MoS_2 η_{norm} multiplied by (i) DDA-calculated field-enhancement factors by the nanoantenna ($\gamma^4\eta_{\text{norm}}$; red line) and (ii) measured SHG enhancement factors ($X\eta_{\text{norm}}$; red squares). The peak measured

https://doi.org/10.1557/mrc.2018.133 Published online by Cambridge University Press

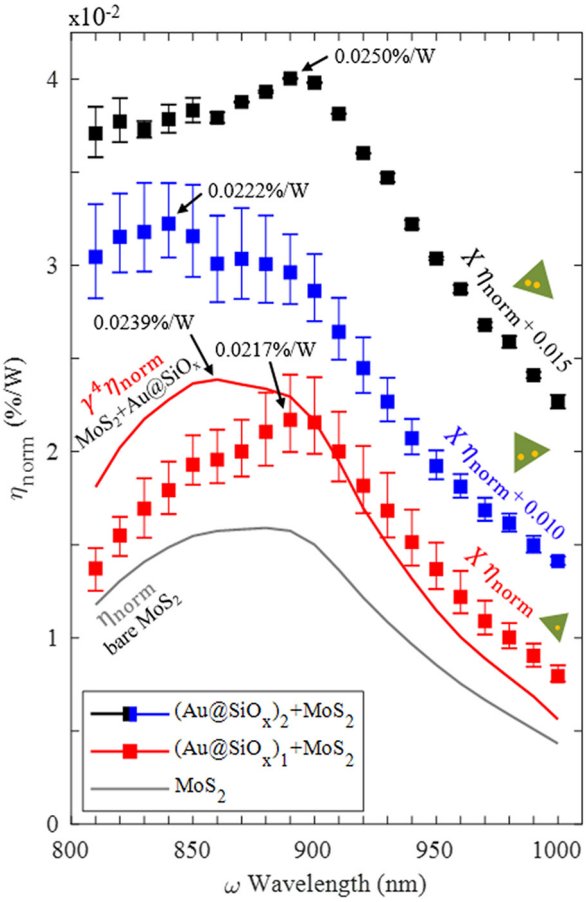


Figure 5. Normalized SHG conversion efficiency, η_{norm}, for a MoS_2 monolayer in the absence [gray line; calculated using Eq. (3)] and presence of a $(Au@SiO_x)_i$ nanoantenna, where subscript i is 1 for the monomer (red square) or 2 for the dimers (blue and black squares). $Au@SiO_x$ nanoantennas were a 15 nm Au shell/120 nm SiO_x core particle. "$\gamma^4\ \eta_{norm}$" (red line) is the calculated enhancement in η_{norm} [see Eq. (2)] using DDA-calculated values of γ for nanoantenna monomer-decorated MoS_2 monolayer. "$X\ \eta_{norm}$" shows measured η_{norm} for the $Au@SiO_x$-MoS_2 heterostructures (squares), where X was the measured SHG enhancement factors relative to MoS_2 controls, under the condition that accrued SHG resulted solely from local field augmentation by the nanoantenna (i.e., $X = \gamma^4$). Note that $X\ \eta_{norm}$ for the 280 nm (blue squares) and 170 nm (black squares) gap dimers are vertically offset by 0.010 and 0.015 units from their absolute magnitudes, respectively, for clarity. The error is the maximum and minimum from the mean from 4 and 2 sample sizes for the monomer and dimer data, respectively.

$X\eta_{norm}$ for the single nanoantenna-MoS_2 heterostructure was 0.0217%/W at 890 nm excitation. Good agreement in magnitude and frequency-dependence is observed at off-resonant wavelengths beyond 880 nm, with an evident dip proximal to the 820 nm LSPR frequency, putatively due to plasmonic losses.

Plasmonic dampening of the pump laser at wavelengths proximal to the 820 nm $Au@SiO_x$ nanoantenna LSPR appeared to diverge measured SHG-enhanced η_{norm} (i.e., $X\eta_{norm}$) of the monomeric heterostructure from its DDA-calculated $\gamma^4\eta_{norm}$ profile. Good agreement was observed at off-resonant excitation wavelengths. It is hypothesized that plasmonic activity of the nanoantenna dampened the pump laser via plasmon-phonon transduction, plasmonic re-radiation in-plane with the MoS_2 and/or 11–38% plasmonic hot electron injection losses.[4,5] For example, frequency-dependent plasmonic re-radiation from a nanoantenna could scatter resonant pump photons away from the MoS_2, thus preventing the production of a SH photon from their annihilation. Plasmonic losses in nanoantenna-TMD heterostructures change the degree to which the pump laser can couple to the TMD, which was not taken into account in Eqs. (1)–(3). Incomplete characterization of these interactions to date precluded quantitation of such pump-TMD coupling effects in presence of plasmonic nanoantennas, but hold interest as future work. At wavelengths beyond 900 nm where plasmonic losses were less appreciable, $X\eta_{norm}$ converged near the calculated $\gamma^4\eta_{norm}$ profile with good agreement in magnitude.

Measured SHG enhancement factors for the dimeric nanoantenna-MoS_2 heterostructures gave $X\eta_{norm}$ profiles in Fig. 5 (scaled vertically by 0.010 and 0.015 units for clarity) that were akin to the monomeric heterostructure sans pump losses, despite their distinct capacitively-coupled plasmonic activity. Interestingly, these dimer $X\eta_{norm}$ data closely resemble their raw SHG measurements in a laboratory setting. The 280 nm-gap (170 nm-gap) dimer enhanced peak $X\eta_{norm}$ from 0.0217%/W for the monomer to 0.0222%/W at 840 nm (0.0250%/W at 890 nm). The largest value of overall $\eta_{2\omega}$ for any measured $Au@SiO_x$ nanoantenna-MoS_2 heterostructure using Eq. (2) was 1.24×10^{-7} at the $I_\omega = 100$ GW/cm^2 employed to collect these data.

Quantitation of γ-factors for the dimers to distinguish contributions from multiple single nanoantennas versus inter-nanoantenna coupled interactions (see Fig. S12) was computationally prohibitive to compare with measured X values. DDA computation time scales with the cube of total target dipoles, (N_{dipole}).[3] The 15 nm thick Au shell necessitated a 3 nm inter-dipole spacing for solution convergence of optical extinction spectra calculations, giving N_{dipole} of 65,257 dipoles for one $Au@SiO_x$ nanoantenna in DDA (excluding any substrate). By comparison, a uniform Au sphere with equal volume to the shell@core nanoantennas would have allowed 98 × reduced computation time with 14,147 dipoles at a 5 nm spacing. Accurate calculation of near-field enhancement magnitudes necessitates ~1 nm spacings, giving 1,767,063 dipoles that further exacerbate computational expense. A boundary element approach may circumvent these obstacles in future work.

Discussion

Plasmonic enhancement of SHG and THG from several nonlinearly-active materials via Au- and Ag-loading/deposition schemes have been studied: ionic polymer bilayer films,[11] organic dyes,[12] silicon carbide nanoparticles,[14] barium titanate nanoparticles,[13] zinc oxide nanowires,[15] rubidium titanyl phosphate,[16] and indium tin oxide.[17] Relative to these materials, 2D TMD offer rich capabilities as a nonlinear

https://doi.org/10.1557/mrc.2018.133 Published online by Cambridge University Press

medium for nano-optoelectronics[10] due to its 2–3 orders-of-magnitude higher $\chi^{(2)}$ of 10^2–10^3 pm/V,[6,7,21,22] mechanical flexibility, direct bandgap near 2 eV, and susceptibility to field gating.[30] For the interested reader, Ref. 10 reviews work to date on enhanced nonlinear responses from 2D TMD after integration with dielectric cavity crystals (spanning SHG, saturable absorption, third-order processes, and exciton–polariton interactions), which is an alternative approach to plasmonic resonances for nonlinear response gain.

This work showed SHG from 2D TMD materials can be augmented by localized plasmon fields supported by metal nanoantennas. The degree of SHG augmentation by single-mode plasmonic nanoantennas, however, remains lower than theoretical potential. Such a difference was acknowledged by Fryett et al. for WSe_2 interfaced with a Si cavity crystal,[18] although recent work by Wang et al. demonstrating >47 × local SHG augmentation has begun to bridge the experiment-theory gap.[19] Similarly, Pu et al. and Zakharko et al. measured 500 × and 72 × plasmon-enhanced SHG from barium titanate and silicon carbide, despite their electrodynamic field simulations suggesting 3500 × and 220 × enhancements were possible, respectively.[13,14] Intrinsic material losses not accounted in continuum electrodynamic models that likely contribute to the shortfall herein may include:

(1) Weak local field enhancement by single nanoantenna seen by the MoS_2 sublayer (see Figure S13) relative to isotropic nanoantenna doping of 3D nonlinear media and/or micron-scale coverage by regular lattices of nanoantenna[11–17]
(2) Reabsorption of SH signal (2.48–3.06 eV) above the MoS_2 bandgap (1.86 eV) featuring high density of states,[18] where classical models cannot simultaneously account for both linear and nonlinear processes
(3) Intrinsic dampening of the pump laser at wavelengths proximal to the nanoantenna LSPR prior to TMD excitation, e.g., via ohmic-relaxation of Landau-damped plasmons, plasmon re-radiation, or trapping of hot electrons/holes into intermediary interface states
(4) Carbon buildup on the MoS_2 and Au surfaces from correlative SEM characterization prior to evaluating SHG performance in the multiphoton microscope
(5) Confounding metrological influences

Energetic conversion of the pump into plasmonic hot electrons injected into the TMD is a quantum mechanical phenomena. Atomistic-level optoelectronic properties and transport at metal-2D semiconductor interfaces remain difficult to account for at the continuum levels interrogated by available measurement techniques. Advancing classical electrodynamic models to accommodate quantum-level metal–TMD interactions could allow improved, multi-scale design and description of such heterostructured hybrid nanomaterials in future work.

Conclusion

Frequency dependence and plasmon-driven intensity enhancements of up to 88% to SHG from $\sim 4 \times 10^5$ nm^2 CVD-synthesized MoS_2 monolayers in the presence of monomeric and dimeric 150 nm Au@SiO_x shell@core nanoantennas were comparable with estimates from *ab initio* theory and DDA simulation. SHG from (i) MoS_2 in the presence of a Au@SiO_x monomer and dimer (170 and 280 nm gaps), (ii) ten MoS_2 controls, and (iii) five Au@SiO_x nanoantenna controls were measured using a 810–1000 nm tunable Ti:Sapphire laser coupled into a multiphoton microscope with hyperspectral imaging. Improved normalized SHG conversion efficiency, η_{norm}, of the nanoantenna-TMD heterostructures was quantitatively consistent with local field augmentation by the 820 nm dipole LSPR of the nanoantenna monomer by comparing (i) measured SHG enhancement with (ii) DDA-calculated enhanced local field strength at the MoS_2 by the nanoantenna. SHG activity of MoS_2 controls in the 810–1000 nm ω range, coinciding with a resonant 2ω interaction with the C exciton transition, followed their DDA-calculated $\chi^{(2)}$ profile and agreed with previous reports. The inversion-symmetric Au@SiO_x nanoantennas did not exhibit SHG in favor of broadband 2ω luminescence from *d*-orbital electrons. A capacitively-coupled plasmon resonance near 960 nm emerged for the 170 nm-gap nanoantenna dimer, which augmented MoS_2 SHG to a peak η_{norm} of 0.0250%/W.

Supplementary material

The supplementary material for this article can be found at https://doi.org/10.1557/mrc.2018.133.

Acknowledgments

This work was supported in part by NSF EEC-1260301, NSF Graduate Research Fellowship awarded to G.T.F, The University of Arkansas Foundation, Walton Charitable Foundation, NCCR MUST instrument of the Swiss National Research Council, and USARL Cooperative Agreement Number W911NF-17-2-0057 award to G.T.F. DDA simulations were performed on the supercomputers of the Arkansas High-Performance Computing Center, supported by NSF 918970 and 959124. The views and conclusions contained in this document are those of the authors and should not be interpreted as representing the official policies, either expressed or implied, of the National Science Foundation, Army Research Laboratory or the US Government. The US Government is authorized to reproduce and distribute reprints for Government purposes notwithstanding any copyright notation herein.

G.T.F. directed the work, performed experiments and data analysis, and drafted text and figures for the manuscript. L.B. and J.-P.W. developed the experimental setup. D.K.R. initiated consideration of nanoantenna-enhanced nonlinear activity in TMD. L.B. and D.K.R. refined compilation of text and figures. The authors acknowledge 2D Semiconductors for supplying CVD MoS_2 samples. The authors thank Drs. Gregory J. Salamo, Surendra P. Singh, Hameed A. Naseem, and Jeremy R. Dunklin for engaging discussions of the data, Dr. Vasyl Kilin for supporting the experiments, and Manoj Seeram for DDA assistance.

https://doi.org/10.1557/mrc.2018.133 Published online by Cambridge University Press

References

1. G.T. Forcherio and D.K. Roper: Spectral characteristics of noble metal nanoparticle-molybdenum disulfide heterostructures. *Adv. Opt. Mater.* **4**, 1288 (2016).
2. E. Palacios, S. Park, S. Butun, L. Lauhon, and K. Aydin: Enhanced radiative emission from monolayer MoS_2 films using a single plasmonic dimer nanoantenna. *Appl. Phys. Lett.* **111**, 031101 (2017).
3. U. Bhanu, M.R. Islam, L. Tetard, and S.I. Khondaker: Photoluminescence quenching in gold-MoS_2 hybrid nanoflakes. *Sci. Rep.* **4**, 5575 (2014).
4. Y. Yu, Z. Ji, S. Zu, B. Du, Y. Kang, Z. Li, Z. Zhou, K. Shi, and Z. Fang: Ultrafast plasmonic hot electron transfer in Au nanoantenna/MoS_2 heterostructures. *Adv. Funct. Mater.* **26**, 6394 (2016).
5. G.T. Forcherio, J.R. Dunklin, C. Backes, Y. Vaynzof, M. Benamara, and D. K. Roper: Gold nanoparticles physicochemically bonded onto tungsten disulfide nanosheet edges exhibit augmented plasmon damping. *AIP Adv.* **7**, 075103 (2017).
6. D.J. Clark, V. Senthilkumar, C.T. Le, D.L. Weerawarne, B. Shim, J.I. Jang, J.H. Shim, J. Cho, Y. Sim, M.-J. Seong, S.H. Rhim, A.J. Freeman, K.-H. Chung, and Y.S. Kim: Strong optical nonlinearity of CVD-grown MoS_2 monolayer as probed by wavelength-dependent second-harmonic generation. *Phys. Rev. B* **90**, 121409 (2014).
7. L.M. Malard, T.V. Alencar, A.P.M. Barboza, K.F. Mak, and A.M. de Paula: Observation of intense second harmonic generation from MoS_2 atomic crystals. *Phys. Rev. B* **87**, 201401 (2013).
8. D. Li, W. Xiong, L. Jiang, Z. Xiao, H. Rabiee Golgir, M. Wang, X. Huang, Y. Zhou, Z. Lin, J. Song, S. Ducharme, L. Jiang, J.-F. Silvain, and Y. Lu: Multimodal nonlinear optical imaging of MoS_2 and MoS_2-based van der Waals heterostructures. *ACS Nano* **10**, 3766 (2016).
9. G.T. Forcherio, J. Riporto, J.R. Dunklin, Y. Mugnier, R.L. Dantec, L. Bonacina, and D.K. Roper: Nonlinear optical susceptibility of two-dimensional WS_2 measured by hyper Rayleigh scattering. *Opt. Lett.* **42**, 5018 (2017).
10. T. Fryett, A. Zhan, and A. Majumdar: Cavity nonlinear optics with layered materials. *Nanophotonics.* **7**, 355 (2017).
11. K. Chen, C. Durak, J.R. Heflin, and H.D. Robinson: Plasmon-enhanced second-harmonic generation from ionic self-assembled multilayer films. *Nano Lett.* **7**, 254 (2007).
12. M. Ishifuji, M. Mitsuishi, and T. Miyashita: Bottom-up design of hybrid polymer nanoassemblies elucidates plasmon-enhanced second harmonic generation from nonlinear optical dyes. *J. Am. Chem. Soc.* **12**, 4418 (2009).
13. Y. Pu, R. Grange, C.L. Hsieh, and D. Psaltis: Nonlinear optical properties of core-shell nanocavities for enhanced second-harmonic generation. *Phys. Rev. Lett.* **104**, 207402 (2010).
14. Y. Zakharko, T. Nychyporuk, L. Bonacina, M. Lemiti, and V. Lysenko: Plasmon-enhanced nonlinear optical properties of SiC nanoparticles. *Nanotechnology* **24**, 055703 (2013).
15. G. Grinblat, M. Rahmani, E. Cortes, M. Caldarola, D. Comedi, S.A. Maier, and A.V. Bragas: High-efficiency second harmonic generation from a single hybrid ZnO nanowire/Au plasmonic nano-oligomer. *Nano Lett.* **14**, 6660 (2014).
16. L. Sánchez-García, C. Tserkezis, M.O. Ramírez, P. Molina, J.J. Carvajal, M. Aguiló, F. Díaz, J. Aizpurua, and L.E. Bausá: Plasmonic enhancement of second harmonic generation from nonlinear $RbTiOPO_4$ crystals by aggregates of silver nanostructures. *Opt. Express* **24**, 8491 (2016).
17. B. Metzger, M. Hentschel, T. Schumacher, M. Lippitz, X. Ye, C.B. Murray, B. Knabe, K. Buse, and H. Giessen: Doubling the efficiency of third harmonic generation by positioning ITO nanocrystals into the hot-spot of plasmonic gap-antennas. *Nano Lett.* **14**, 2867 (2014).
18. T.K. Fryett, K.L. Seyler, J. Zheng, C. Liu, X. Xu, and A. Majumdar: Silicon photonic crystal cavity enhanced second-harmonic generation from monolayer WSe_2. *2*D Mater. **4**, 015031 (2016).
19. Z. Wang, Z. Dong, H. Zhu, L. Jin, M.-H. Chiu, L.-J. Li, Q.-H. Xu, G. Eda, S. A. Maier, A.T.S. Wee, C.-W. Qiu, and J.K.W. Yang: Selectively plasmon-enhanced second-harmonic generation from monolayer tungsten diselenide on flexible substrates. *ACS Nano* **12**, 1859 (2018).
20. A.R. Klots, A.K.M. Newaz, B. Wang, D. Prasai, H. Krzyzanowska, D. Caudel, N.J. Ghimire, J. Yan, B.L. Ivanov, K.A. Velizhanin, A. Burger, D.G. Mandrus, N.H. Tolk, S.T. Pantelides, and K.I. Bolotin: Probing excitonic states in ultraclean suspended two-dimensional semiconductors by photocurrent spectroscopy. *Sci. Rep.* **4**, 6608 (2014).
21. C.Y. Wang and G.Y. Guo: Nonlinear optical properties of transition-metal dichalcogenide MX_2 (M = Mo, W; X = S, Se) monolayers and trilayers from first-principles calculations. *J. Phys. Chem. C* **119**, 13268 (2015).
22. M.L. Trolle, G. Seifert, and T.G. Pedersen: Theory of excitonic second-harmonic generation in monolayer MoS_2. *Phys. Rev. B* **89**, 235410 (2014).
23. N. Mao, Y. Chen, D. Liu, J. Zhang, and L. Xie: Solvatochromic effect on the photoluminescence of MoS_2 monolayers. *Small* **9**, 1312 (2013).
24. B. Mukherjee, F. Tseng, D. Gunlycke, K. Kumar, G. Eda, and E. Simsek: Complex electrical permittivity of the monolayer molybdenum disulfide (MoS_2) in near UV and visible. *Opt. Mater. Express* **5**, 447 (2015).
25. S. Palomba, M. Danckwerts, and L. Novotny: Nonlinear plasmonics with gold nanoparticle antennas. *J. Opt. Pure Appl. Opt.* **11**, 114030 (2009).
26. G.F. Walsh and L. Dal Negro: Enhanced second harmonic generation from Au nanoparticle arrays by femtosecond laser irradiation. *Nanoscale* **5**, 7795 (2013).
27. M.D. McMahon, D. Ferrara, C.T. Bowie, R. Lopez, and R.F. Haglund Jr: Second harmonic generation from resonantly excited arrays of gold nanoparticles. *Appl. Phys. B* **87**, 259 (2007).
28. S. Kadkhodazadeh, J.R. De Lasson, M. Beleggia, H. Kneipp, J.B. Wagner, and K. Kneipp: Scaling of the surface plasmon resonance in gold and silver dimers probed by EELS. *J. Phys. Chem. C* **118**, 5478 (2014).
29. S.C. Kumar, G.K. Samanta, K. Devi, and M. Ebrahim-Zadeh: High-efficiency, multicrystal, single-pass, continuous-wave second harmonic generation. *Opt. Express* **19**, 11152 (2011).
30. K.L. Seyler, J.R. Schaibley, P. Gong, P. Rivera, A.M. Jones, S. Wu, J. Yan, D.G. Mandrus, W. Yao, and X. Xu: Electrical control of second-harmonic generation in a WSe_2 monolayer transistor. *Nat. Nanotechnol.* **10**, 407 (2015).

https://doi.org/10.1557/mrc.2018.133 Published online by Cambridge University Press